Letters

An Integrated Inductive Power and Capacitive Data Transfer System Using Ultrathin Nanocrystalline Laminated Sheets

Guangyu Yan, *Graduate Student Member, IEEE*, Binhong Cao, *Graduate Student Member, IEEE*,
Jie Deng, *Student Member, IEEE*, and Zhicheng Guo, *Member, IEEE*

***Abstract*—This letter proposes a novel system that exploits 0.9 mm-thick nanocrystalline (NC) laminated sheets to integrate inductive power transfer (IPT) with capacitive data transfer. Besides enhancing inductive coupling and providing magnetic shielding, the NC laminated sheets can also enable capacitive coupling for data transfer through the parasitic capacitances, benefiting from the high electrical conductivity of NC material. Compared to those similar solutions, the NC laminated sheets combine the functions of ferrite plates and metal plates, enabling a more compact system. A 100-W prototype is established with 97.2% power transfer efficiency and 1-Mbps data rate. The operation of data transfer has almost no impact on power efficiency, and the interference from the power channel to data channel is sufficiently low, which guarantees the correct recovery of data bits.**

***Index Terms*—Capacitive data transfer, inductive power transfer (IPT), nanocrystalline (NC) laminated sheets, parasitic capacitances, power efficiency.**

I. Introduction

Inductive power transfer (IPT) enables galvanic isolation and provides great convenience by eliminating physical connections. Wireless communication is required in many IPT systems for real-time monitoring and close-loop control. Traditional techniques such as Bluetooth and Wi-Fi could introduce millisecond-level time delay, thereby limiting their suitability. To overcome this, researchers have developed various special methods of data transfer [1] as alternatives.

Inductive methods are commonly used to achieve data transfer, mainly including signal injection and extra inductive coupling. Signal injection methods [2] involve complex circuit design to suppress power-to-data interference due to the shared transfer channel, whereas extra inductive coupling methods [3] require another pair of coils for data transfer, which could increase the size and weight of the system. Capacitive coupling is another way to achieve data transfer. In [4], the parasitic capacitances among the split aluminum plates are utilized to form capacitive coupling, whereas the work in [5] employs the parasitic capacitances between the coils and between the aluminum plates. The data transfer channel in [5] is directly connected to coils, which might cause significant interference to data signal under high-power level of IPT.

Nanocrystalline (NC) has been selected as an alternative to ferrite in transformer design [6] and IPT systems [7] owing to its higher permeability, saturation flux density and thermal conductivity. Recently, NC laminated cores and sheets have gained wide attention, as the lamination structure can effectively mitigate eddy current loss by restricting the path of eddy currents. In this proposed system, "FINEMET" NC laminated sheets are employed not only to enhance inductive coupling and provide magnetic shielding, but also to establish capacitive coupling for data transfer by leveraging the high-electrical-conductivity NC layers as electrode plates. The main contributions are as follows.

1) The data transfer is achieved without introducing extra components into the original IPT, and thus the impact on power transfer is negligible.
2) The NC laminated sheets functionally replace both ferrite and metal plates in [4], [5], and [9] owing to the high permeability and high conductivity of NC material, enabling a more compact and lightweight system with less components.
3) 97.2% high-power efficiency and 1-MHz high-data rate are realized, outperforming those similar solutions [4], [5], [9].

II. Integrated Inductive Power and Capacitive Data Transfer System

A. System Overview

The system diagram is depicted in Fig. 1(a), where each side contains a circular coil and two rectangular sheets split from a single 100×100 mm NC laminated sheet, with only 0.9 mm thickness and only 32 g mass. A small gap of 1 mm is left between the two rectangular sheets on each side. The lamination direction is perpendicular to the coil plane. The IPT is realized through a *CLLC* resonant converter with dual-active-synchronization (DAS) modulation [8], which applies identical driving signals to the H-bridges on both sides.

Received 15 August 2025; revised 26 October 2025 and 16 November 2025; accepted 20 November 2025. Date of publication 24 November 2025; date of current version 19 January 2026. *(Corresponding author: Zhicheng Guo.)*

The authors are with Power Electronics and Energy Conversion (PEEC) Lab, Arizona State University, Tempe, AZ 85212 USA (e-mail: guangyuy@asu.edu; binhongc@asu.edu; jdeng56@asu.edu; zhicheng.guo@asu.edu).

Color versions of one or more figures in this article are available at https://doi.org/10.1109/TPEL.2025.3636455.

Digital Object Identifier 10.1109/TPEL.2025.3636455

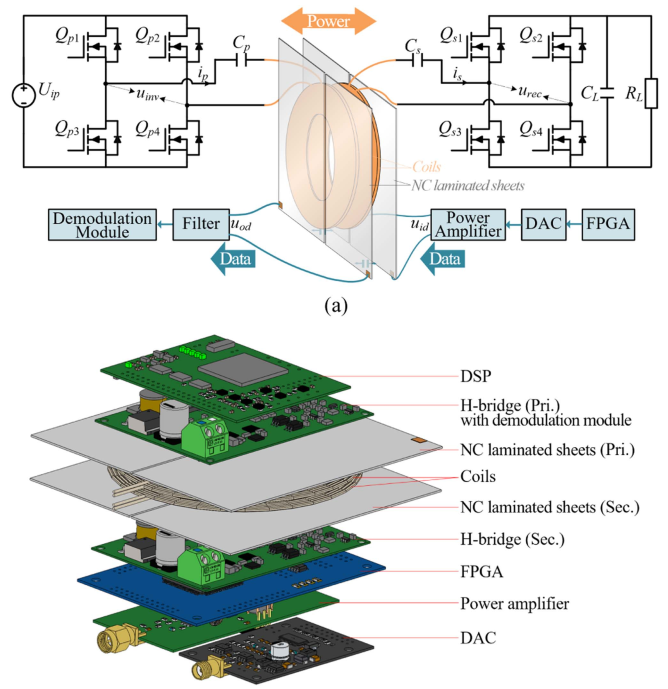

(a)

(b)

Fig. 1. Overview of the proposed integrated power and data transfer system. (a) Schematic diagram. (b) Exploded view of the hardware.

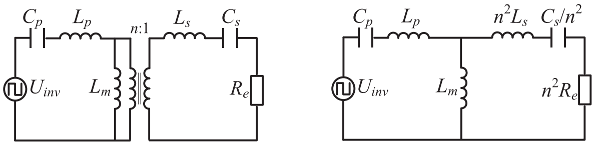

(a) (b)

Fig. 2. Equivalent circuit of the *CLLC* resonant converter. (a) Simplified circuit. (b) Further simplified circuit.

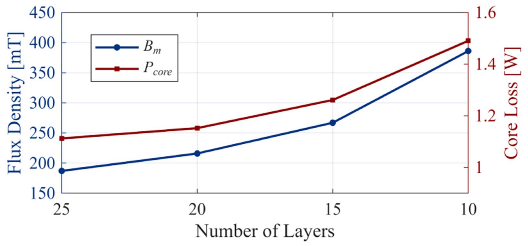

Fig. 3. Maximum flux density and core loss with respect to the number of NC layers in the NC laminated sheets.

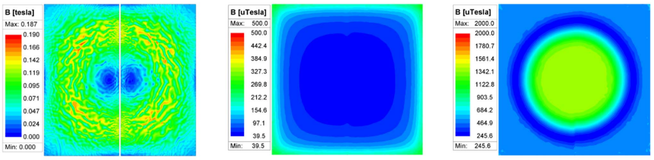

(a) (b) (c)

Fig. 4. Magnetic flux density distribution on (a) inner surface of the NC laminated sheets; (b) 100×100 mm area (inside the transformer) located 3 mm away from the NC laminated sheets; and (c) 100×100 mm area (outside the transformer) located 3 mm away from the NC laminated sheets.

On the secondary side for data transmission, an field-programmable gate array (FPGA), a digital-to-analog converter and a (PA) are cascaded to generate 2ASK signal according to the data bits. The PA output is connected to the NC layers of the two secondary-side sheets. On the primary side for data reception, a band-pass filter is followed by a 2ASK demodulation module, with the filter input connected to the NC layers of the two primary-side sheets. Due to the parasitic capacitances, the four connected NC layers together with the two coils form a six-plate capacitive coupling structure, in which the parasitic capacitances between the facing sheets positively contribute to data transfer. An exploded view of the overall system is shown in Fig. 1(b).

B. Inductive Power Transfer

The *CLLC* resonant converter is capable of bidirectional dc–dc conversion, consisting of two active H-bridges and two individual inductor-capacitor resonant tanks connected to the primary and secondary sides of a transformer. Taking the forward mode as an example, the equivalent circuit is shown as Fig. 2(a), where n is the turns ratio of the transformer, L_m is the magnetizing inductance, L_p and L_s are the leakage inductances, and C_p and C_s are the resonant capacitors that resonate with L_p and L_s, respectively. In this work, the turns ratio is set to 1:1. The H-bridge rectifier with the load R_L can be equivalently modeled as R_e equal to $8R_L/\pi^2$. The equivalent circuit can be further simplified to Fig. 2(b). Accordingly, the voltage gain of the converter can be expressed as follows:

$$G_{pf} = \left| \frac{n^2(R_e + Z_{Ls} + Z_{Cs})||Z_{Lm}}{Z_{Lp} + Z_{Cp} + n^2(R_e + Z_{Ls} + Z_{Cs})||Z_{Lm}} \cdot \frac{R_e}{R_e + Z_{Ls} + Z_{Cs}} \right| \tag{1}$$

where Z_{Lp}, Z_{Cp}, Z_{Ls}, Z_{Cs}, and Z_{Lm} are the impedances of L_p, C_p, L_s, C_s, and L_m, respectively. When the converter is operating at the resonant frequency, the voltage gain is equal to $1/n$ and independent of the load [10]. An optimal dead time is set to ensure ZVS turn-ON for the H-bridges on both sides to minimize the switching loss.

The NC laminated sheets exhibit anisotropic permeability and electrical conductivity, with significant differences between lamination and nonlamination directions. Each NC laminated sheet utilized in this system includes 25 NC layers, 25 resin layers, and 2 cover films. Using homogenization method in the finite element analysis (FEA) simulation software, the magnetic flux is analyzed and the core loss in the sheets is evaluated. In the transformer with the same external excitation (i.e., emulating the prototype *CLLC* converter), as the number of NC layers decreases from 25 to 10, both the maximum flux density and core loss in the NC sheets increase, as illustrated in Fig. 3. Nevertheless, the maximum flux density is always well below the very high-saturation flux density 1.23 T. Fig. 4(a) shows the magnetic flux density distribution on the inner surface of

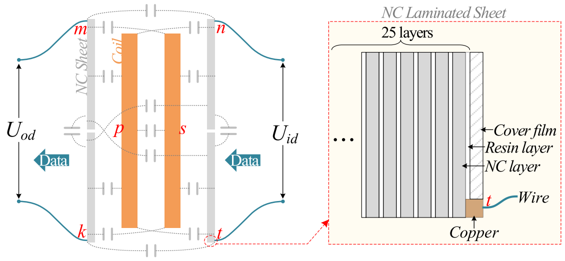

Fig. 5. Parasitic capacitors among the electrode plates.

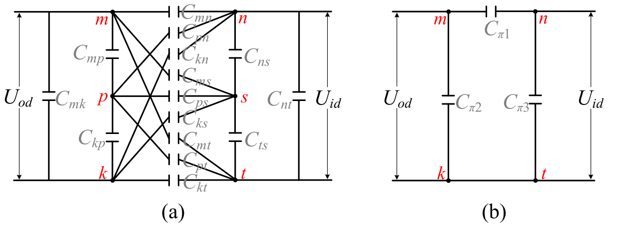

(a) (b)

Fig. 6. Circuit model of capacitive coupling. (a) Original model. (b) π-shaped simplified model.

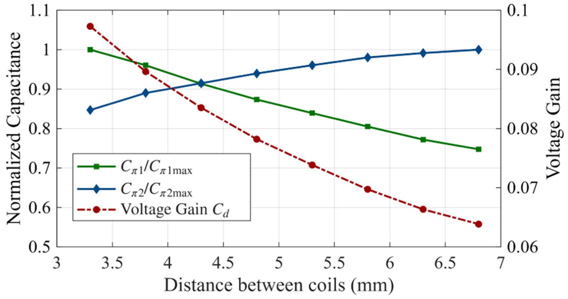

Fig. 7. Normalized equivalent capacitances and voltage gain for data transfer versus the distance between coils, with the NC sheet-to-coil distance kept constant.

the 25-layer NC sheets. In addition, the NC sheets also provide effective magnetic shielding. At the center of a 100 × 100 mm area, which is 3 mm away from the primary-side NC sheets, the flux density in air is reduced by nearly 35 times compared to that inside the transformer, as shown in Fig. 4(b) and (c), thereby mitigating EMI to these PCBs in the system.

C. Capacitive Data Transfer

The NC layers can be considered as electrode plates due to high electrical conductivity. As shown in Fig. 5, to facilitate wire connection, a small portion of the cover film and resin layer is removed to expose the underlying NC layer in each sheet. A piece of copper foil is attached to the exposed NC, and the litz wire is soldered onto the copper foil. The resulting wire-connected NC layers of the four sheets, together with the two coils, which can be treated as metal plates, form a six-plate capacitive coupling model containing numerous parasitic capacitors. The other NC layers in each sheet are not connected to any circuit, and thus they are floating with no applied voltage. However, they have an influence on the value of these established capacitances.

The wire-connected NC layers of the four sheets are denoted by m, n, k, and t, while the two coils are denoted by p and s. Nodes n and t constitute the input port of data signal, whereas m and k constitute the output port. Hence, the data can be transferred from the secondary side to primary side.

The capacitive cross-coupling is illustrated by Fig. 6(a). Because of the symmetric structure, the following equalities hold: $C_{mn} = C_{kt}$, $C_{mk} = C_{nt}$, $C_{mp} = C_{ns} = C_{kp} = C_{ts}$, $C_{ms} = C_{pn} = C_{pt} = C_{ks}$, and $C_{kn} = C_{mt}$. It should be noted that these equalities may deviate slightly in practice due to imperfect symmetry. According to [4], the model in Fig. 6(a) can be simplified to a π-shaped model comprising only three equivalent capacitors as shown in Fig. 6(b). Considering the above equalities, the three equivalent capacitors can be derived as follows:

$$C_{\pi 1} = (C_{mn} - C_{mt})/2 \tag{2}$$

$$C_{\pi 2} = C_{\pi 3} = C_{mk} + C_{mt} + \left(\frac{C_{mp} + C_{ms}}{2}\right). \tag{3}$$

The voltage gain G_{d} of data transfer can be expressed as follows:

$$G_d = \frac{U_{od}}{U_{id}} = \frac{\frac{1}{j\omega_d C_{\pi 2}}}{\frac{1}{j\omega_d C_{\pi 1}} + \frac{1}{j\omega_d C_{\pi 2}}} = \frac{C_{\pi 1}}{C_{\pi 1} + C_{\pi 2}}. \tag{4}$$

Equations (2) to (4) indicate that only the parasitic capacitances between the NC layers of the facing sheets (i.e., C_{mn} and C_{kt}) facilitate data transfer, while the others weaken the received data signal. When the coil-to-coil distance is 3.3 mm and the NC sheet-to-coil distance is 6 mm, the equivalent capacitances $C_{\pi 1}$ and $C_{\pi 2}$ ($= C_{\pi 3}$) are 0.9 pF and 8.4 pF, respectively, resulting in a voltage gain G_d of 0.097. With increasing coil-to-coil distance while remaining constant NC sheet-to-coil distance, the voltage gain G_d decreases markedly, as illustrated in Fig. 7. To ensure correct data demodulation, the received data signal should exceed the threshold of the demodulation circuit with sufficient signal-to-noise ratio. Therefore, the voltage gain G_d should not be too low, and the spacing distance should be properly constrained. In the prototype, the amplitude of the received data signal needs to be at least 0.9 V, indicating that the voltage gain should be higher than 0.075 when the amplitude of input voltage is 12 V. According to Fig. 7, the coil-to-coil distance should be within 5 mm. Nevertheless, the constrained distance also depends on the lateral size of the NC laminated sheets, which means that a larger sheet area can support a greater data transfer distance.

III. EXPERIMENTAL VERIFICATION

An experimental prototype is built up to verify the proposed system. The transformer and the H-bridge are shown in Fig. 8. The main parameters for the *CLLC* resonant converter and capacitive data transfer are listed in Table I. Gallium nitride (GaN) high-electron-mobility transistors (HEMTs) (GS61004B) are employed to construct the H-bridge inverter and rectifier under DAS modulation. C0G multilayer ceramic capacitors are used

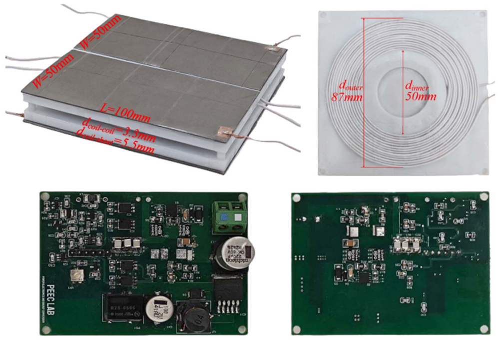

Fig. 8. NC sheets-based transformer and PCB of GaN HEMT H-bridge with demodulation module.

TABLE I
Main Parameters of the Proposed System

	Parameters	Value
Power Transfer	Switching frequency f_s	200 kHz
	Magnetizing inductance L_m	31.1 μH
	Leakage inductance L_p/L_s	3.3 μH
	Resonant capacitance C_p/C_s	192 nF
	Load resistance R_L	29.8 Ω
	Input DC voltage U_{ip}	54.8 V
	Coil turns	14:14
	Coupling coefficient k	0.91
Data Transfer	Carrier frequency f_d	17 MHz
	Equivalent capacitance $C_{\pi1}$	0.9 pF
	Equivalent capacitance $C_{\pi2}/C_{\pi3}$	8.4 pF
	Transmitted data signal $U_{id,pk}$	12 V

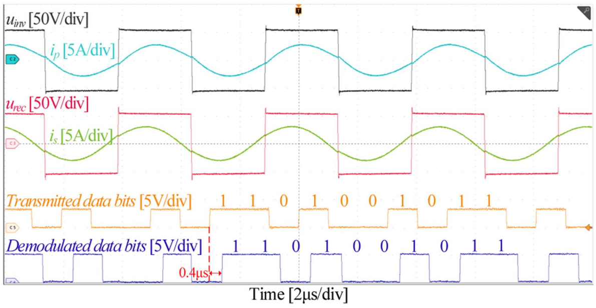

Fig. 9. Waveforms of simultaneous power and data transfer.

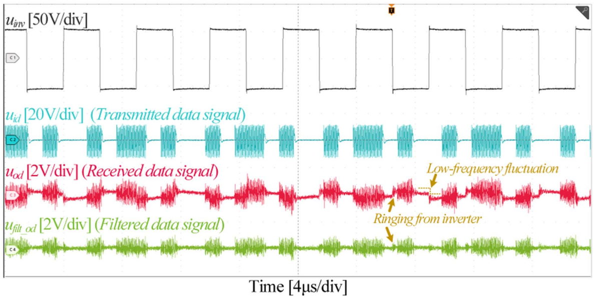

Fig. 10. Waveforms of the inverter output voltage and the data signal.

as resonant capacitors because of their low equivalent series resistance.

Fig. 9 validates the simultaneous transfer of power and data. The upper four waveforms refer to the output voltage and current of the inverter (i.e., u_{inv} and i_p), and the input voltage and current of the rectifier (i.e., u_{rec} and i_s). u_{rec} is close to u_{inv}, which is consistent with the theoretical *CLLC* converter design. The lower two waveforms show the transmitted data bits and the finally demodulated data bits, which are well matched with a time delay of only 0.4 μs. Each data bit lasts for 1 μs, corresponding to a data transfer rate of 1 Mbps.

The waveforms during the intermediate stages of data transfer are shown in Fig. 10. To demonstrate where the interference is from, the output voltage of the inverter is displayed on the top for reference. The lower three waveforms represent: 1) the transmitted data signal in response to data bits (i.e., input voltage of capacitive coupling u_{id}); 2) received data signal (i.e., output voltage of capacitive coupling u_{od}); and 3) filtered data signal u_{filt_od}. The measured voltage gain of data transfer is 0.0916, only slightly smaller than the theoretically calculated value in Section II, which verifies the effectiveness of the analysis and design.

Two types of interference can be clearly observed on the waveform of u_{od}. The first is the 200 kHz square-wave fluctuation originating from the power signal itself. The second is the small high-frequency ringing caused by the switches of the inverter, which occurs periodically corresponding to the edges of inverter output voltage. After the band-pass filter, the square-wave interference is effectively eliminated due to its much lower frequency compared with the data signal. However, the ringing is difficult to filter out, as its frequency is close to the data signal's frequency. When the input voltage of the power transfer increases, the ringing becomes more pronounced. Once it reaches a certain level, it will affect the data demodulation, resulting in error data bits.

To evaluate the dc-dc power efficiency of the *CLLC* resonant converter at different frequency, the resonant capacitors on both sides were adjusted to vary the resonant frequency from 80 kHz to 440 kHz in steps of 40 kHz. The switching frequencies of the inverter and rectifier were kept equal to the corresponding resonant frequency. The measured dc-dc efficiency versus frequency is presented in Fig. 11(a), with a constant input power of 100 W. The efficiency first increases with the frequency, reaches a peak around 240 kHz, and then gradually decreases. Given the very little efficiency variation between 200 kHz and 280 kHz, 200 kHz is selected as the default working frequency for power transfer to maximize the frequency gap between power and data transfer, thereby suppressing the interference to the data receiving port. At 200 kHz, the measured dc-dc efficiency is 97.2%, and the power loss breakdown is depicted in Fig. 11(b). In addition, when evaluating how power transfer is influenced by the data transfer, it is found that the power efficiency remains nearly unchanged at 97.2% whether the data transfer is active or not.

Table II presents a detailed comparison between the proposed system and several reported systems. The main comparison focuses on [4], [5], [9], and [11] that adopt capacitive coupling for data transfer. Compared to [4], [5], and [9], the proposed system achieves higher data rate while employing fewer components. Although [11] achieves the same data rate as ours and

TABLE II
Comparison Between Different Works

	Method for Data Transfer	Components (excluding coils for power transfer)	Data Rate	Power Efficiency	Max Output Power	Coil Size	Medium
This work	Capacitive coupling	2(i)	1 Mbps	97.2%	97 W	87mm diameter	Air
[4]	Capacitive coupling	4(ii)	9.6 kbps	86.9%	50 W	100mm square	Air
[5]	Capacitive coupling	4(ii)	230 kbps	79.6%	40 W	90mm diameter	Air
[9]	Capacitive coupling	4(ii)	600 kbps	91.4%	145 W	180mm square	Air
[11]	Capacitive coupling	2(iii)	1 Mbps	91%	1.2 kW	250mm square	Seawater
[3]	Extra inductive coupling	4(iv)	1 Mbps	94.3%	884 W	200mm square	Seawater
[12]	Signal injection	4(v)	2 Mbps	93.4%	1.1 kW	200mm square	Freshwater

(i)A pair of NC laminated sheets. (ii)A pair of ferrite plates and a pair of metal plates. (iii)Two additional transformers for data transfer.
(iv)An extra pair of coils and a pair of ferrite plates. (v)Four additional transformers for data transfer

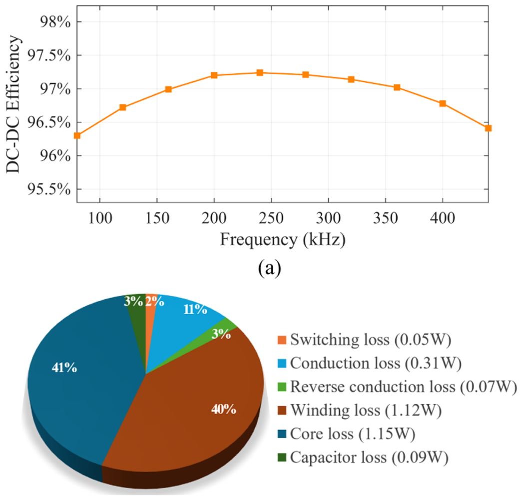

(a)

(b)

Fig. 11. DC-DC power efficiency of the *CLLC* resonant converter. (a) Efficiency versus frequency. (b) Loss breakdown at 200 kHz.

does not employ magnetic sheets or metal plates for capacitive coupling, the absence of these components leads to weaker inductive coupling and a lack of shielding effect. The number of additional components for each system is listed in the table with the note specifying the components used, which demonstrates the advantage of the proposed system in using fewer components and the benefits of the NC laminated sheets for multifunctional integration. Moreover, due to the adoption of GaN HEMTs rectifier instead of diode-based rectifier, the proposed system exhibits the highest power efficiency among the compared systems.

IV. CONCLUSION

By leveraging both the high permeability and high conductivity of NC material, the NC laminated sheets in the proposed system serve as multipurpose components for both IPT and capacitive data transfer. The system can enable wireless transfer of sensed information such as temperature, voltage, and current, allowing real-time monitoring and closed-loop control with very low time delay.

Experimental results demonstrate that the system achieves high power efficiency over 97% across the 160–360 kHz frequency range at an input power of 100 W. There is almost no decrease in power efficiency during the concurrent transfer of power and data. The data transfer rate reaches 1 Mbps with zero bit error rate, owing to the minimal interference from the power transfer and the well-designed filter. The proposed system outperforms those similar solutions in terms of power efficiency and data rate while using fewer components.

REFERENCES

[1] Y. Yao, P. Sun, X. Liu, Y. Wang, and D. Xu, “Simultaneous wireless power and data transfer: A comprehensive review,” *IEEE Trans. Power Electron.*, vol. 37, no. 3, pp. 3650–3667, Mar. 2022.

[2] Y. Wang, T. Li, M. Zeng, J. Mai, P. Gu, and D. Xu, “An underwater simultaneous wireless power and data transfer system for AUV with high-rate full-duplex communication,” *IEEE Trans. Power Electron.*, vol. 38, no. 1, pp. 619–633, Jan. 2023.

[3] C. Da, L. Wang, F. Li, C. Tao, and Y. Zhang, “Analysis of undersea simultaneous wireless power and 1 Mb/s data rate transfer system based on DDQ coil,” *IEEE Trans. Power Electron.*, vol. 38, no. 10, pp. 11814–11825, Oct. 2023.

[4] X. Yang et al., “A cost-effective implementation of independent data and power transmission channels in wireless power transfer systems,” *IEEE Trans. Circuits Syst. II, Exp. Briefs*, vol. 69, no. 3, pp. 1532–1536, Mar. 2022.

[5] X. Li, C. Tang, X. Dai, P. Deng, and Y. Su, “An inductive and capacitive combined parallel transmission of power and data for wireless power transfer systems,” *IEEE Trans. Power Electron.*, vol. 33, no. 6, pp. 4980–4991, Jun. 2018.

[6] W. Shen, F. Wang, D. Boroyevich, and C. W. Tipton IV, “High-density nanocrystalline core transformer for high-power high-frequency resonant converter,” *IEEE Trans. Ind. Appl.*, vol. 44, no. 1, pp. 213–222, Jan./Feb. 2008.

[7] Y. Wang, C. Q. Jiang, C. Chen, T. Ma, X. Li, and T. Long, “Hybrid nanocrystalline ribbon core and flake ribbon for high-power inductive power transfer applications,” *IEEE Trans. Power Electron.*, vol. 39, no. 1, pp. 1898–1911, Jan. 2024.

[8] Y. Cao, M. Ngo, R. Burgos, A. Ismail, and D. Dong, “Switching transition analysis and optimization for bidirectional CLLC resonant DC transformer,” *IEEE Trans. Power Electron.*, vol. 37, no. 4, pp. 3786–3800, Apr. 2022.

[9] G. Yan, W. Han, C. Liu, B. Zhang, and M. Li, “A simultaneous wireless power and full-duplex data transfer system using a mix of inductive and capacitive couplings,” *IEEE Trans. Circuits Syst. II, Exp. Briefs*, vol. 72, no. 1, pp. 323–327, Jan. 2025.

[10] P. He and A. Khaligh, “Comprehensive analyses and comparison of 1 kW isolated DC–DC converters for bidirectional EV charging systems,” *IEEE Trans. Transp. Electrific.*, vol. 3, no. 1, pp. 147–156, Mar. 2017.

[11] T. Li, Z. Sun, Y. Wang, J. Mai, and D. Xu, “Undersea simultaneous wireless power and data transfer system with extended communication distance and high rate,” *IEEE Trans. Power Electron.*, vol. 39, no. 3, pp. 2917–2921, Mar. 2024.

[12] T. Li, Z. Sun, Y. Wang, J. Mai, and D. Xu, “Simultaneous wireless power and data transfer system with full-duplex MIMO communication channels for underwater applications,” *IEEE Trans. Ind. Electron.*, vol. 20, no. 4, pp. 6382–6393, Apr. 2024.